The effects of smoothing length on the onset of wave breaking in smoothed particle hydrodynamics (SPH) simulations of highly directionally spread waves

Kanehira, Taiga; McAllister, Mark L.; Draycott, Samuel; Nakashima, Takuji; Ingram, David M.; van den Bremer, Ton S.; Mutsuda, Hidemi

DOI
10.1007/s40571-022-00463-z

Publication date
2022

Document Version
Final published version

Published in
Computational Particle Mechanics

Citation (APA)
Kanehira, T., McAllister, M. L., Draycott, S., Nakashima, T., Ingram, D. M., van den Bremer, T. S., & Mutsuda, H. (2022). The effects of smoothing length on the onset of wave breaking in smoothed particle hydrodynamics (SPH) simulations of highly directionally spread waves. *Computational Particle Mechanics*, *9*(5), 1031-1047. https://doi.org/10.1007/s40571-022-00463-z

Computational Particle Mechanics
https://doi.org/10.1007/s40571-022-00463-z

The effects of smoothing length on the onset of wave breaking in smoothed particle hydrodynamics (SPH) simulations of highly directionally spread waves

Taiga Kanehira[1] · **Mark L. McAllister**[2] · **Samuel Draycott**[3] · **Takuji Nakashima**[1] · **David M. Ingram**[4] · **Ton S. van den Bremer**[5,6] · **Hidemi Mutsuda**[1]

Received: 14 June 2021 / Revised: 10 January 2022 / Accepted: 13 January 2022

Abstract

Ocean wave breaking is a difficult-to-model oceanographic process, which has implications for extreme wave statistics, the dissipation of wave energy, and air–sea interaction. Numerical methods capable of reliably simulating real-world directionally spread breaking waves are useful for investigating the physics of wave breaking and for the design of offshore structures and floating bodies. Smoothed particle hydrodynamics is capable of modelling highly steep and overturning free surfaces, which makes it a promising method for simulating breaking waves. This paper investigates the effect of smoothing length on simulated wave breaking in both following and crossing seas. To do so, we reproduce numerically the experiments of highly directionally spread breaking waves in McAllister et al. (J Fluid Mech 860:767–786, 2019. https://doi.org/10.1017/jfm.2018.886) using a range of normalised smoothing lengths: $h/d_p = 1.4, 1.7, 2.0, 2.3$, with h smoothing length and d_p particle spacing. The smallest smoothing length we use appears to adversely affect the fidelity of the simulated surface elevation, so that the tallest wave crest observed in experiments is not fully reproduced (coefficient of determination $r^2 \approx 0.7$). For smoothing lengths $h/d_p = 1.7$, 2.0, and 2.3, the experiments are well reproduced ($r^2 \geq 0.88$); in these simulations smoothing length predominantly affects the spatial extent and duration of breaking. Qualitative and quantitative comparison of our simulations shows that values of h/d_p in the range 1.7−2 best reproduce the wave breaking phenomena observed in experiments.

Keywords Smoothed particle hydrodynamics · Wave breaking · Smoothing length · Intermediate water depth · Directional spreading · Crossing seas

1 Introduction

Wave breaking in the ocean can cause significant damage to vessels as well as coastal and offshore structures. Furthermore, wave breaking plays an important role in the dissipation of wave energy and the exchange of momentum fluxes between the upper ocean and atmosphere [1]. Therefore, accurate prediction of wave breaking is of great importance in coastal and ocean engineering and physical oceanography.

Computational fluid dynamics (CFD) has been used to explore complex breaking phenomena such a jet formation [2–5], eddy generation [6–9], turbulent transport [10], and to predict violent hydrodynamic loads on offshore structures [11–16]. High-fidelity numerical reproduction of complex breaking phenomena is challenging and computationally demanding. However, numerical models can provide a greater level of physical insight than laboratory experi-

✉ Hidemi Mutsuda
mutsuda@hiroshima-u.ac.jp

[1] Graduate School of Advanced Science and Engineering, Hiroshima University, Higashi-Hiroshima, Japan

[2] Department of Engineering Science, University of Oxford, Oxford OX1 3PJ, UK

[3] Department of Mechanical, Aerospace and Civil Engineering, University of Manchester, Manchester M13 9PL, UK

[4] School of Engineering, University of Edinburgh, Edinburgh EH9 3FB, UK

[5] Department of Engineering Science, University of Oxford, Oxford OX1 3PJ, UK

[6] Faculty of Civil Engineering and Geosciences, Delft University of Technology, 2628 CD Delft, The Netherlands

ments, in which certain quantities (i.e. fluid velocities and multi-valued free surfaces) are difficult to measure. To model steep overturning waves, Lagrangian particle-based methods offer certain advantages when compared to Eulerian grid-based methods [17]. Using Lagrangian meshless approaches, large free surface deformations can be simulated without the need to explicitly model the free surface, such as in the Volume of Fluid (VOF) method [18] and the level-set method [19]. Eulerian grid-based approaches often struggle with steep and overturning free surfaces and violent breaking, and re-meshing may be necessary for large deformations at the interface (e.g. [20]). In Lagrangian models, convection terms may be calculated without numerical diffusion, which is unavoidable in grid-based methods. Hence, particle-based methods, such as smoothed particle hydrodynamics (SPH) [21,22] and the moving particle semi-implicit (MPS) method [23], have been applied to a variety of wave breaking simulations [2,6,7,24,25]. Moreover, in particle-based methods, physical boundaries such as wavemakers may be readily simulated using Dynamic Boundary Particles (DBPs) [26], which allows for the creation of a numerical wave tank.

There are two principal variants of the SPH method, namely the weakly compressive SPH (WCSPH) method [27] and incompressible SPH (ISPH) method [28]. The former is an explicit method, and fluid pressure can be computed from an equation of state to link density with pressure. In case of the ISPH method, the pressure filed may be implicitly computed by solving a pressure Poisson equation based on the projection method [29]. Compared to ISPH, the WCSPH method is fully explicit process and easy to program [30] and widely implemented on graphics processing units (GPU) [31,32]. In the WCSPH context, unphysical pressure noise and numerical stability are major issue (e.g. [33]). Various numerical schemes exist to address this issue; for example, an artificial viscous term in the momentum equation [34], a Lagrangian kernel [35], and density diffusive term on the continuity equation [36] are proposed in the WCSPH model. Delta-SPH schemes have been widely adapted to coastal and ocean engineering problems (see [37]). Recent advantages for tensile instability [38] from negative pressure are also reported [39,40] by employing both of delta-SPH and particle shifting techniques (see, for example, [41,42]). Further, the delta-SPH techniques with background mesh scheme have proposed in [43], by which accurate pressure field and precise reproduction of free surface are enhanced. In this paper, we use the WCSPH code DualSPHysics with a delta-SPH scheme proposed in [36].

Since Monaghan [27] first extended the SPH method to free surface flows, particle-based methods have been applied to study wave breaking, particularly in the surf zone [5,44–47]. A recent review of the SPH method applied to free surface flows can be found in [17]. Breaking in the surf zone can generate complex rotational fluid motion and vortices. To represent turbulence at sub-particle scale, following the large-eddy simulation (LES) concept, Goto et al. [48] introduced the sub-particle scale (SPS) turbulence model in the MPS method developed by [23]. Dalrymple and Rogers [49] have also integrated an SPS approach into a viscous SPH formulation to simulate breaking waves on beaches and to assess the resulting vorticity. Using the DualSPHysics SPH solver [50], Roselli et al. [51] conducted long-duration simulations in order to investigate the ability of their model to simulate consecutive periodic waves in the surf zone. Lowe et al. [7] also used DualSPHysics to model plunging and spilling wave breaking and investigate wave set-up and currents in the surf zone. Accurate tracking of the free surface is an issue of major concern in breaking simulations. In [52], Khayyer et al. proposed a corrected incompressible SPH (CISPH) method and investigated the tracking accuracy of the free surface of waves breaking on a uniform slope.

Choice of model parameters such as the smoothing length and coefficient of viscosity is important in achieving high-fidelity simulations, and the effects of such parameters are particularly pronounced when simulating complex unstable processes like wave breaking. Padova et al. [53] considered the ratio between particle spacing d_p and smoothing length h for regular wave breaking on a constant slope and found that $d_p/h = 0.7$ was the best value for their simulations. Roselli et al. [54] proposed Metamodel-Embedded Evolutionary framework and found the set of parameters that provide an accurate reproduction of a second-order Stokes wave. Lowe et al. [7] also carefully investigated how various model parameters such as the smoothing coefficient ($coefh$) and the coefficient of artificial viscosity (α) affect reproduction of spilling wave breaking. They found that the values of $coefh = 1.2$ and $\alpha = 0.01$ were optimal for their simulations. However, we note that these sensitivity analyses are limited to wave propagation in 2D. The authors are unaware similar studies in carried out for similar 3D simulations, perhaps as a result the associated high computational cost.

The majority of breaking wave simulations performed using particle-based methods have been performed for unidirectional problems, most often located in the surf zone [44–47]. Ocean waves are often significantly directionally spread [55,56], and of these directionally spread waves crossing conditions are considered to be a pernicious example [57–60]. As reported in the experiments of [61] (hereinafter referred to as MC19), the form breaking takes in crossing conditions is fundamentally different from so-called following-sea or unidirectional conditions; horizontal breaking with overturning of crests in a following sea can limit wave height and steepness, but vertical jet-like breaking in a crossing sea does not do so to the same extent. In MC19, the Draupner wave [62] was reproduced at scale in the circular wave basin (diameter $D = 25$ m and water depth $d = 2$ m), FloWave, located at the University of Edinburgh [63]. MC19 concluded that this change in breaking behaviour may have played a key role in the formation of the Draupner wave, indicating that further research is required to understand the limiting conditions and wave breaking in crossing seas. To this end, SPH simulations aimed at reproducing the experiments in MC19 were carried out in [64]. Good agreement was found between wave gauge measurements and simulated surface elevations, and it was concluded that existing kinematic and geometric breaking criteria are difficult to apply in highly directionally spread conditions.

In this paper, we present additional simulations to those in [64] to investigate how the ratio between smoothing length h and particle spacing d_p affects the simulation of directionally spread breaking waves in intermediate to deep water ($d = 2$ m, $k_p d \approx 1.8$ with k_p the peak wavenumber). We examine how smoothing length affects the onset, spatial extent and duration of wave breaking. To do so, we use an SPH model of the 25 m diameter circular FloWave basin developed using DualSPHysics [50,65], previously reported in [64,66,67]. To assess the performance of the model, we compare with experiments in MC19 as in [64].

The present paper is laid out as follows. In this study, we used DualSPHysics (v5.0). The numerical method and settings we used are explained in Sect. 2. Subsequently, a qualitative and quantitative comparison between simulations and experiments is made for four h/d_p values in Sect. 3. In Sect. 3.1, we qualitatively examine the effect of varying h/d_p on wave breaking in following and crossing conditions. In Sect. 3.2, we quantitatively compare the four cases with different h/d_p to the experiments of MC19 using values of the coefficient of determination of the free surface. We then analyse the temporal and spatial extent of wave breaking using the vertical component of individual fluid particle acceleration in Sect. 3.3. Finally, conclusions are drawn in Sect. 4.

2 Numerical method

2.1 SPH fundamentals

In the SPH method [21,22], a continuous fluid flow can be discretised as a set of interpolation points called particles that move in conjunction with the fluid motion. Physical quantities of the fluid continuum such as pressure, density, and velocity components can be obtained at each particle location using spatial interpolation between neighbouring particles with a smoothing length h.

The fundamental principle of the SPH method is to approximate a physical quantity ϕ as follows:

$$\phi(\boldsymbol{r}) = \int_{\Omega} \phi(\boldsymbol{r}') W(|\boldsymbol{r} - \boldsymbol{r}'|, h) \mathrm{d}\boldsymbol{r}', \tag{1}$$

where $\boldsymbol{r}$ is the focused position vector, $\boldsymbol{r}'$ is the position vector of neighbouring particles, Ω is the volume within which interaction with neighbouring particles is considered, h is the smoothing length and corresponds to the radial length scale of Ω, and W is the kernel function. Equation 1 can be converted into discrete form,

$$\phi(\boldsymbol{r}_a) = \sum_{b=1}^{N} \phi(\boldsymbol{r}_b) W(|\boldsymbol{r}_b - \boldsymbol{r}_a|, h) V_b, \tag{2}$$

where a is a discrete particle, V_b is the volume of a neighbouring particle b, and $V_b = m_b/\rho_b$, with m and ρ representing the mass and density of particle b, respectively. In this study, we use the quintic Wendland kernel ([68]), which is expressed as

$$W(q, h) = \alpha_{\mathrm{D}} \left(1 - \frac{q}{2}\right)^4 (2q + 1), \qquad 0 \le q \le 2, \tag{3}$$

where $q = r/h$ is given by the distance between any two selected particles (r) divided by the smoothing length h, and α_{D} is equal to $7/(4\pi h^2)$ in 2D, and $21/(16\pi h^3)$ in 3D.

2.2 Governing equations

The DualSPHysics code solves the Navier–Stokes equations to describe the motion of a viscous incompressible fluid. Using Eq. (2) in accordance with [49], conservation of mass and momentum in discrete SPH form can be expressed as

$$\frac{\mathrm{d}\rho_a}{\mathrm{d}t} = \sum_b m_b (\boldsymbol{u}_a - \boldsymbol{u}_b) \cdot \nabla_a W_{ab} + \mathcal{D}_a, \tag{4}$$

$$\begin{aligned} \frac{\mathrm{d}\boldsymbol{u}_a}{\mathrm{d}t} = &-\sum_b m_b \left(\frac{p_b}{\rho_b^2} + \frac{p_a}{\rho_a^2}\right) \nabla_a W_{ab} + \boldsymbol{g} \\ &+ \sum_b m_b \left(\frac{4\nu_0 \boldsymbol{r}_{\mathrm{ab}} \cdot \nabla_a W_{ab}}{(\rho_a + \rho_b)(|\boldsymbol{r}_{\mathrm{ab}}|^2 + \zeta^2)}\right) (\boldsymbol{u}_a - \boldsymbol{u}_b) \\ &+ \sum_b m_b \left(\frac{\vec{\tau}_b}{\rho_b^2} + \frac{\vec{\tau}_a}{\rho_a^2}\right) \cdot \nabla_a W_{ab}, \end{aligned} \tag{5}$$

where $\boldsymbol{u}$ is the velocity vector of particles, $\vec{\boldsymbol{\tau}}$ is the SPS stress tensor, $\zeta^2 = 0.01h^2$, $\nu_0 = 1.0 \times 10^{-6}$ m^2/s is the kinematic viscosity of water, $\boldsymbol{r}_{\mathrm{ab}} = \boldsymbol{r}_a - \boldsymbol{r}_b$, and $\mathcal{D}_a$ in Eq. (4) represents a density diffusion term, known as the delta-SPH scheme [36] which is written as,

$$\mathcal{D}_a = \delta h c_0 \sum_b \psi_{ab} \cdot \nabla_a W_{ab} V_b, \tag{6}$$

by which the noise in the pressure field can be reduced. We used the delta-SPH coefficient $\delta = 0.1$, and c_0 is the speed of sound. The ψ_{ab} in Eq. (6) is expressed as

$$\psi_{ab} = 2\left(\frac{\rho_a}{\rho_b} - 1\right)\frac{(\boldsymbol{r}_a - \boldsymbol{r}_b)}{|\boldsymbol{r}_a - \boldsymbol{r}_b|^2 + \zeta^2}, \tag{7}$$

In Eq. (5), the third term on the right-hand side represents the laminar viscosity, as presented in [69], and the fourth term on the right-hand side is the SPS turbulence term formulated in weakly compressible SPH by [49], which is written as

$$\frac{\vec{\tau}_{ab}}{\rho} = \nu_t\left(2S_{ab} - \frac{2}{3}k\delta_{ab}\right) - \frac{2}{3}C_I\Delta^2\delta_{ab}\,|S_{ab}|^2. \tag{8}$$

where $\nu_t = (C_s\Delta)^2\,|S|$ represents the eddy viscosity based on the Smagorinsky model, k is the SPH turbulence kinetic energy, Δ is the initial particle spacing, and $|S| = \sqrt{2S_{ab}S_{ab}}$ in which S_{ab} is the element of SPS strain tensor. We use the Smagorinsky constant ($C_s = 0.12$) and $C_I = 0.0066$ (default values in DualSPHysics) following [49].

2.3 Equation of state for pressure

If we assume our fluid is weakly compressible, pressure can be computed using Tait's equation of state that relates density to pressure as follows:

$$p = b\left[\left(\frac{\rho}{\rho_0}\right)^\gamma - 1\right]. \tag{9}$$

where $\gamma = 7$ and $b = c_0^2\rho_0/\gamma$, $\rho_0 = 1000$ kg/m^3 is the reference density, and $c_0 = 20\sqrt{gd}$ is the speed of sound. Consequently, pressure can be computed by an explicit algorithm, which reduces computational costs compared to solving Poisson's equation using an implicit method.

2.4 Numerical basin model and numerical set-up

Below we describe the numerical tank we used for reproduction of the experimental conditions in MC19. The numerical basin, which is based on the FloWave Ocean Energy Research Facility wave tank at the University of Edinburgh, was developed in [66]. Figure 1 shows a plan view and cross section of the numerical wave tank, which has a 25-m-diameter and 2-m-deep fluid domain. Using 168 hinged-flap-type wavemakers shown as grey segments in Fig. 1, the basin can generate directionally spread waves as well as unidirectional waves as modelled in [66,67]. The bottom boundary in our model and the tank floor are slightly different; the SPH model has a flat boundary, whilst the actual tank has current circulation gratings located on the tank floor at the base of the wave paddles. However, please note that the difference between our SPH model and experimental bottom boundary condition will not affect our simulation results. The waves we have simulated are in intermediate to deep water, and the difference in bottom boundary conditions is limited to the current gratings (not the entire domain). For boundary condition (i.e. the tank floor and wavemakers), we used the Dynamic Boundary Particles (DBPs) proposed in [26]; all 168 hinged-flap wavemakers and the fixed-bottom floor are composed of DBPs. Each of the paddles in the model is made to follow the angles of the actual wavemakers recorded in each of the experiments in MC19, meaning that, in principle, wave generation is implemented exactly as in the experiments.

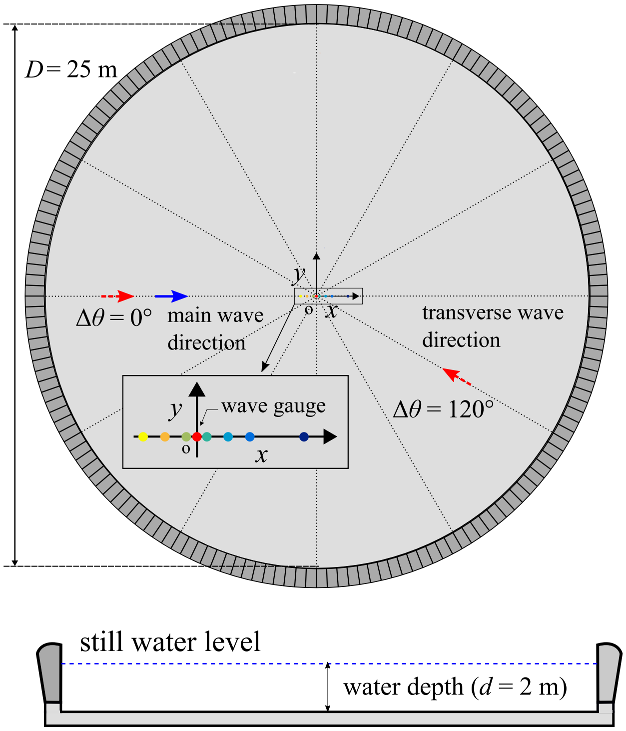

Fig. 1 Geometry and coordinate system of the basin. The arrangement of eight wave gauges at the centre of the basin (coloured cross) is that in MC19. The blue arrow shows the main wave group's direction, and the red-dashed arrows indicate the two mean directions simulated for the transverse wave group (modified from [64]). (Color figure online)

In MC19, the time series measured at the Draupner platform by [62] was decomposed into two wave systems, which cross each other (a main and a transverse wave system; see MC19 for details). Experiments in MC19 were carried out for three scenarios, setting the angle between the two systems $\Delta\theta$ to 0° (following-sea conditions, i.e. no crossing), 60°, and 120°. Both wave systems are directionally spread about their respective mean directions with a wrapped normal spreading function of width 30° applied to the amplitude distribution. Here, two of the experiments of MC19, for following ($\Delta\theta = 0°$) and crossing ($\Delta\theta = 120°$) conditions, are simulated, as illustrated by the red arrows in Fig. 1. In the simulated wave fields, water surface elevations were measured using eight wave gauges located at the centre of basin. A zoomed-in diagram of the gauge array is shown in Fig. 1, and their positions are listed in Table 2.

To investigate the effect of smoothing length h on the simulation of wave breaking, we vary h/d_p from 1.4 to 2.3 by varying h and keeping d_p constant for both experiment (Cases 1–4 for the following sea, and Cases 5–8 for the crossing sea). The initial particle spacing (d_p) used was 0.02 m, which corresponds to H_D/d_p value of 37, where H_D is the wave height of the largest wave measured during experiments. The number of particles required to fill the domain was 127 million in all simulations. A value of $h/d_p = 1.7$ was used in [64,66,67]. The H_D/d_p and d_p used in this study are the same as the finest resolution simulations in [64]. Note that in [64] we have performed a convergence study by varying the initial particle spacing and thus the total number of particles, but have kept the ratio of smoothing length to initial particle spacing constant at $h/d_p = 1.7$. The total run time for each simulation is shown in Table 1. As the value of h/d_p increases, the computational time also significantly increases. Increasing h increases the size of the kernel and hence the time to calculate all particle–particle interactions. It took twice as much time to run simulations using $h/d_p = 2.3$ as it did to run simulations using $h/d_p = 1.7$. For all simulations in this study, we also used the symplectic scheme [70] for time stepping, based on previous findings in [66]. In each time iteration, a variable time step Δt is computed based on [45]. Due to high computational cost, we have set the Courant–Friedrichs–Lewy (CFL) coefficient as 0.4 which is used to multiply Δt.

Table 1 Wave conditions, numerical parameters, and simulation run time

Case	$\Delta\theta$	H_D/d_p	N_p ($\times 10^6$)	h/d_p	Run time (hrs)
1	0°	37	127	1.4	134
2				1.7	167
3				2.0	241
4				2.3	346
5	120°	37	127	1.4	132
6				1.7	167
7				2.0	252
8				2.3	332

GPU: NVIDIA Quadro RTX 8000

Table 2 Position of the wave gauges

WG	1	2	3	4	5	6	7	8
x (m)	− 0.5	− 0.3	− 0.1	0	0.1	0.3	0.5	1
y (m)	0	0	0	0	0	0	0	0

3 Results and discussion

3.1 Simulated wave breaking

Figure 2 shows rendered images of the SPH model of the FloWave tank, with the two images depicting snapshots of simulations for $\Delta\theta = 0°$ and $\Delta\theta = 120°$ in which steep waves can be observed at the centre of tank ($x = 0, y = 0$). In the case of the following sea ($\Delta\theta = 0°$), the main and transverse wave groups also shown in Fig. 1 propagate in the same mean direction from left to right, whereas in the crossing sea ($\Delta\theta = 120°$), the transverse waves cross the centre of the basin from bottom right to top left, as also depicted by the red arrow.

Figures 3 and 4 present still images of the wave breaking observed in the four simulations with different h/d_p values. In these figures, the colour scale denotes the magnitude of the velocity vector at the free surface. In MC19, plunging breaking with crest overturning occurred in the following sea ($\Delta\theta = 0°$). Our results in the case of $\Delta\theta = 0°$ clearly show plunging breaking for all four values of h/d_p. As the waves focus ($t = 24.0$ s), the forward face of the wave steepens in panel (a–d), and a jet emerges which plunges forwards and overturns, as clearly shown in panel (f). Then, as the jet re-attaches and collides with the surface, secondary jet formation occurs and splashing is observed in panels (i–l).

In the crossing simulations in Fig. 4, a large and steep wave crest forms in panels (f–h) for all smoothing lengths except $h/d_p = 1.4$ (e), in which the wave crest height is noticeably reduced, and it is not clear if breaking is occurring in both times presented (e,i). In panel (j,k,f) with large h/d_p values, however, apparent partial breaking occurs after the time of focus ($t = 24.5$ s).

3.2 Sensitivity to smoothing length

In Figs. 5 and 6, we compare simulated free surface elevation to measurements made in MC19 at wave gauge 4 ($x = 0$, $y = 0$) in both experiments (Fig. 5 for $\Delta\theta = 0°$, and Fig. 6 for $\Delta\theta = 120°$) with four different h/d_p values. Excluding for $h/d_p = 1.4$, the simulated free surface elevations ($h/d_p = 1.7$, 2.0 and 2.3) compare well with the experiments. In [53], a value of h/d_p (d_p/h) close to 1.4 (0.7) was recommended. For our simulations, a value of 1.4 appears to result in the underestimation of the large wave crest in both experiments. The difference between our results and [53] may be a consequence of different ratios of wave height to particle spacing (H/d_p). The ratio H/d_p in [53] was 5 ($= 0.11/0.022$), whereas the value we used is approximately 37 ($= 0.73/0.02$) for the maximum wave height (H_D) and is 12 ($0.24/0.02$) for the average wave height ($\bar{H}$) in the crossing sea, where $\bar{H}$ was calculated using wave heights measured at all wave gauges during time $t = 5$ - 32 s. A sen-

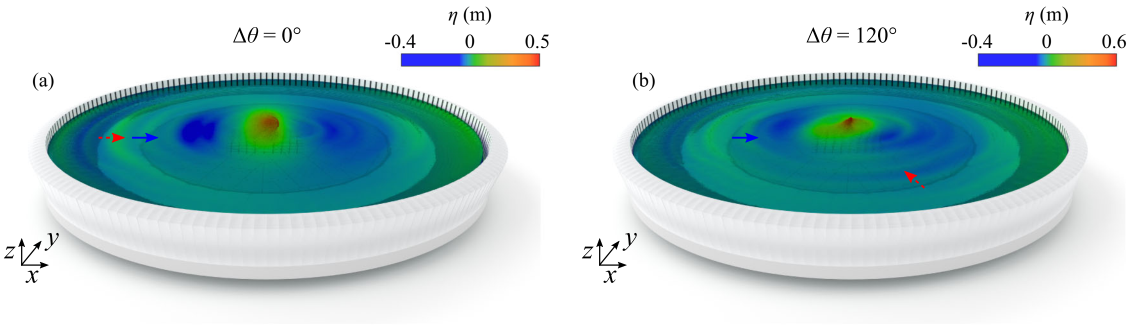

Fig. 2 Examples of simulated wave fields at the time of focus ($t = 24$ s) in the following (**a**) and crossing seas (**b**). The blue and red-dashed arrows show the main and transverse wave groups' directions, respectively, as depicted in Fig. 1. The colour scale corresponds to the value of the surface elevation. (Color figure online)

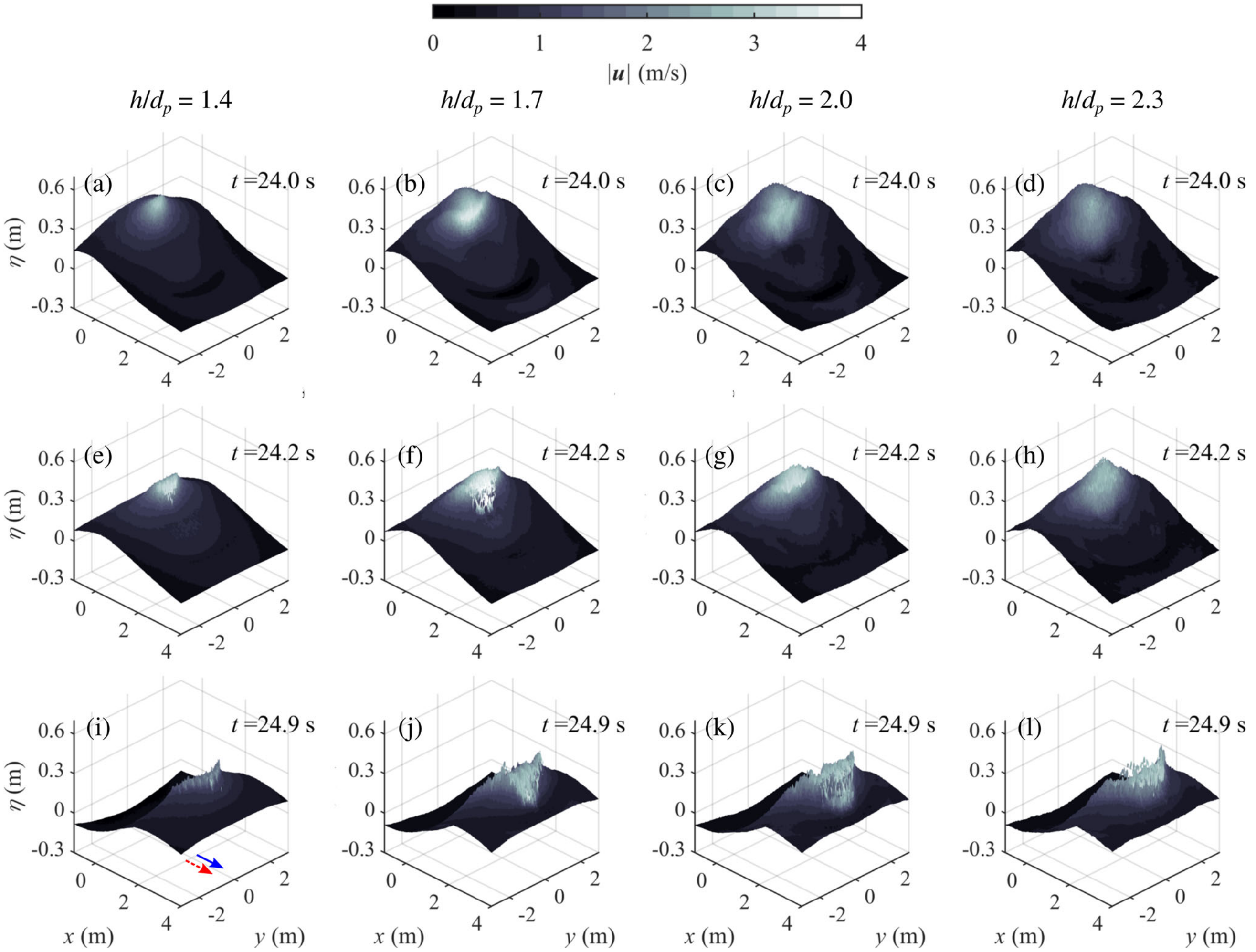

Fig. 3 Series of still images showing the wave breaking observed in our simulations for different values of h/d_p for the following sea ($\Delta\theta = 0°$). Rendered images are presented for 24.0 s, 24.2 s and 24.9 s for h/d_p = 1.4 (**a, e, i**), 1.7 (**b, f, j**), 2.0 (**c, g, k**) and 2.3 (**d, h, l**). The blue and red-dashed arrows in (**i**) mark the main and transverse waves shown in Fig. 1. The colour scale corresponds to the value of the magnitude of the velocity vector at the free surface. (Color figure online)

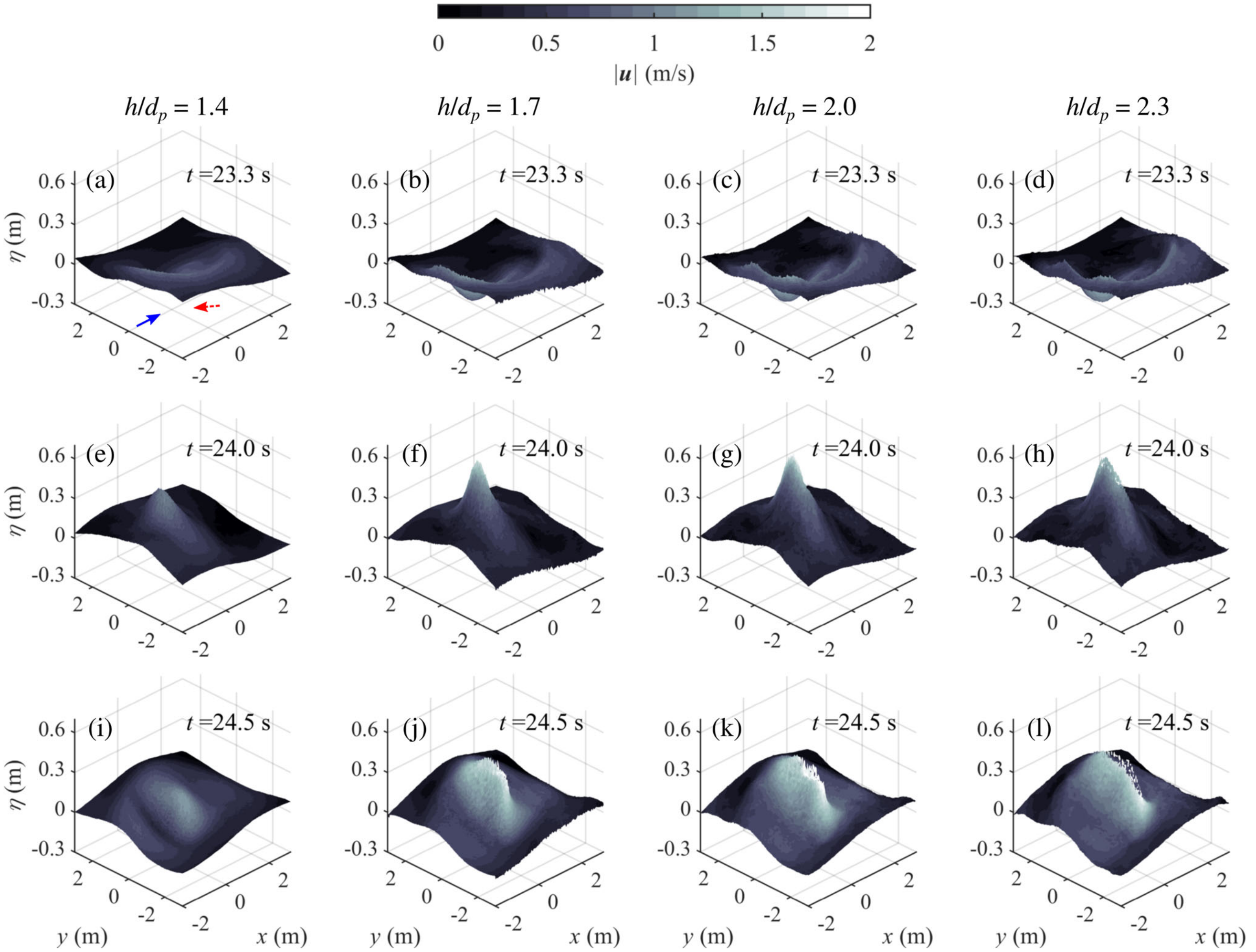

Fig. 4 Series of still images showing the wave breaking observed in our simulations for different values of h/d_p for the crossing sea ($\Delta\theta = 120°$). Rendered images are presented for 23.3 s, 24.0 s and 24.5 s for h/d_p = 1.4 (**a, e, i**), 1.7 (**b, f, j**), 2.0 (**c, g, k**) and 2.3 (**d, h, l**). The blue and red-dashed arrows in (**a**) mark the main and transverse waves shown in Fig. 1. The colour scale corresponds to the value of the magnitude of the velocity vector at the free surface. (Color figure online)

sitivity analysis of wave breaking simulations using a higher ratio ($H/d_p \approx 50$) than in our simulations can be found in [7]. They used a h/d_p value of 1.7, which is also the value that results in the smallest difference between our numerical results and the experiments of MC19.

Figure 7 shows the coefficient of determination (r^2) for the four smoothing lengths h/d_p used in our simulations. We calculate the coefficient of determination r^2 using time series between $t = 23$ and 25 s, corresponding to the main crest, in panels (a) and (b), and over the entire simulation in (c). In panel (a), r^2 values at wave gauges (wave gauge) 1–5 are close to 1. At wave gauges 6, 7, and 8, values decrease slightly. The waves propagate from wave gauges 1 to 8, and as the wave crest approaches the downstream gauges, breaking will have occurred. The influence of smoothing length on r^2 is most pronounced at these downstream gauges (excluding in simulations where $h/d_p = 1.4$), although all values of r^2 are still greater than 0.9. This suggests that smoothing length has an observable effect on the simulation of wave breaking. We note that the water surface will become vertical and double valued as breaking occurs, which may introduce uncertainty in the measurements produced at these gauges.

For the simulations of the crossing sea ($\Delta\theta = 120°$) in Fig. 7b, r^2 values are slightly lower than in the following sea ($\Delta\theta = 0°$), and the effects of smoothing length are more pronounced. This may be a result of the extreme spatial localisation of the main wave crest. Additionally, as the waves do not propagate along the direction of the wave gauges ($y = 0$), a clear distinction between gauges where the wave has and has not broken, as observed in Fig. 7a, does no longer exist. However, the r^2 values are lowest at wave gauges 1 and 8 which are farthest from the point of focus. Figure 7c shows

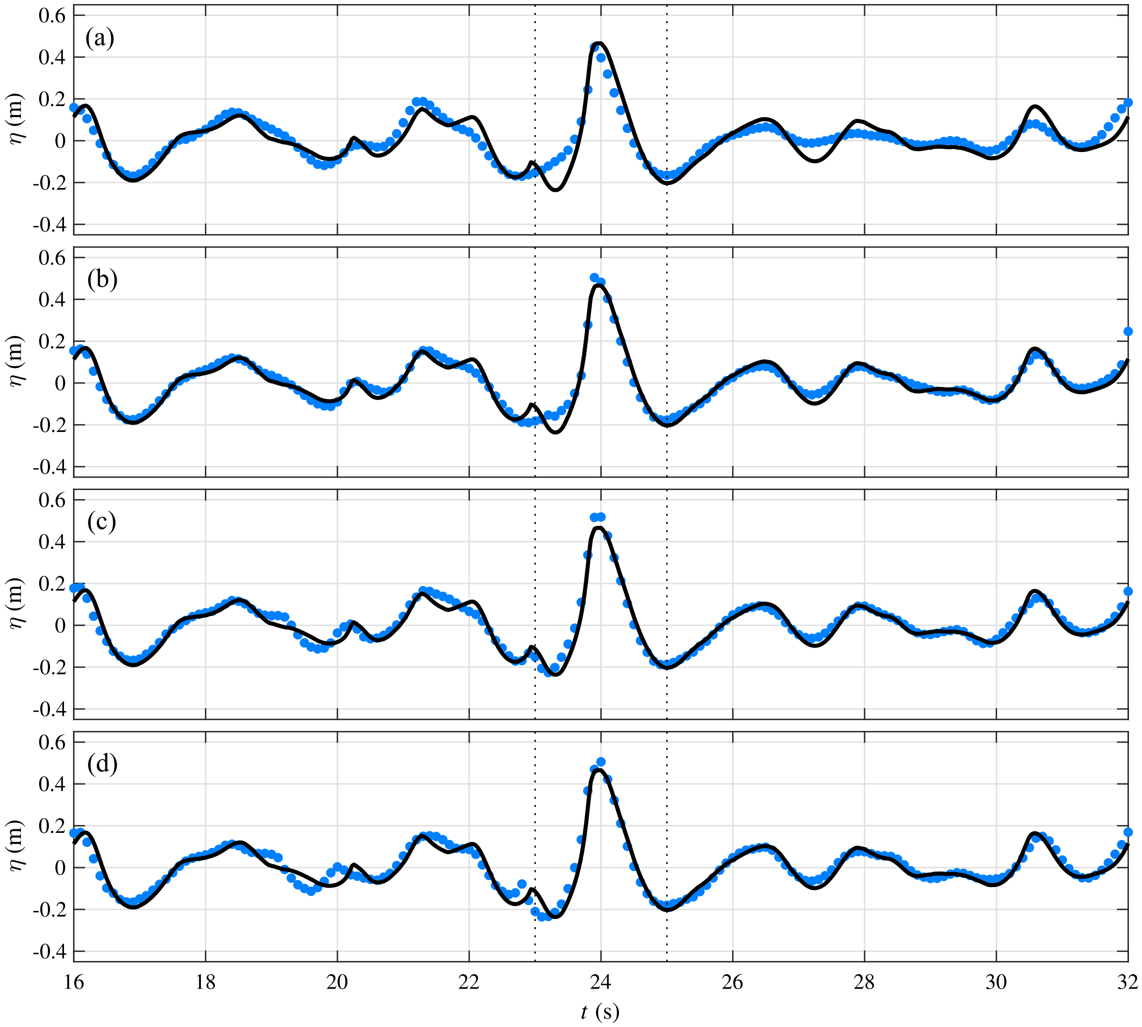

Fig. 5 Time series of surface elevation measured at wave gauge 4 ($x = 0$, $y = 0$) with four different h/d_p values of 1.4 (**a**), 1.7 (**b**), 2.0 (**c**), and 2.3 (**d**) in the following sea ($\Delta\theta = 0°$). Black lines denote the experimental measurements from MC19 and blue dots the SPH results. Vertical dotted lines ($t = 23$–25 s) denote the time interval used to estimate r^2 in Fig. 7a, b. (Color figure online)

r^2 values obtained from the entire simulation (t =0–32 s), showing that r^2 values in the crossing sea ($\Delta\theta = 120°$) are slightly lower than those in the following sea ($\Delta\theta = 0°$). Figure 7a–c demonstrates that the simulations carried out with $h/d_p = 1.7$ reproduce the experimental measurements best for both $\Delta\theta = 0$ and 120°.

When comparing time series of surface elevation alone, simulations carried out for the values of $h/d_p \geq 1.7$ may appear to be very similar. To assess how h/d_p affects simulated wave breaking and jet formation, we compare still images captured during the experiments of MC19 to our simulations in Fig. 8. In Fig. 8, the wave gauge locations are highlighted by vertical dashed blue and red lines and are aligned, so they correspond to those in the images of the experiments (panels a and f). For $\Delta\theta = 0$, in the left-hand column in Fig. 8, simulated surfaces have been plotted at the point where the plunging jet re-attaches to the free surface, as this provides a quantifiable breaking feature to compare between the simulations. The point at which the jet re-attaches to the free surface is significantly different for the different values of h/d_p. As h/d_p increases, the re-attachment point of the jet moves forward in both space and time. Using this measure to compare to the experiments, $h/d_p = 1.7$ and 2.0 appear to produce breaking which is most qualitatively similar to the breaking observed in the experiments. The plunging jet re-attaches to the free surface at approximately the same position as in the experiments ($x \approx 1.3-1.5$ m). For $\Delta\theta = 120°$, shown in the right-hand column in Fig. 8, we show free surface elevation at time $t = 24.0$ s. Clear jet formation and re-attachment do not occur in all of these simulations as wave breaking in the crossing sea is more spatially localised making its reproduction

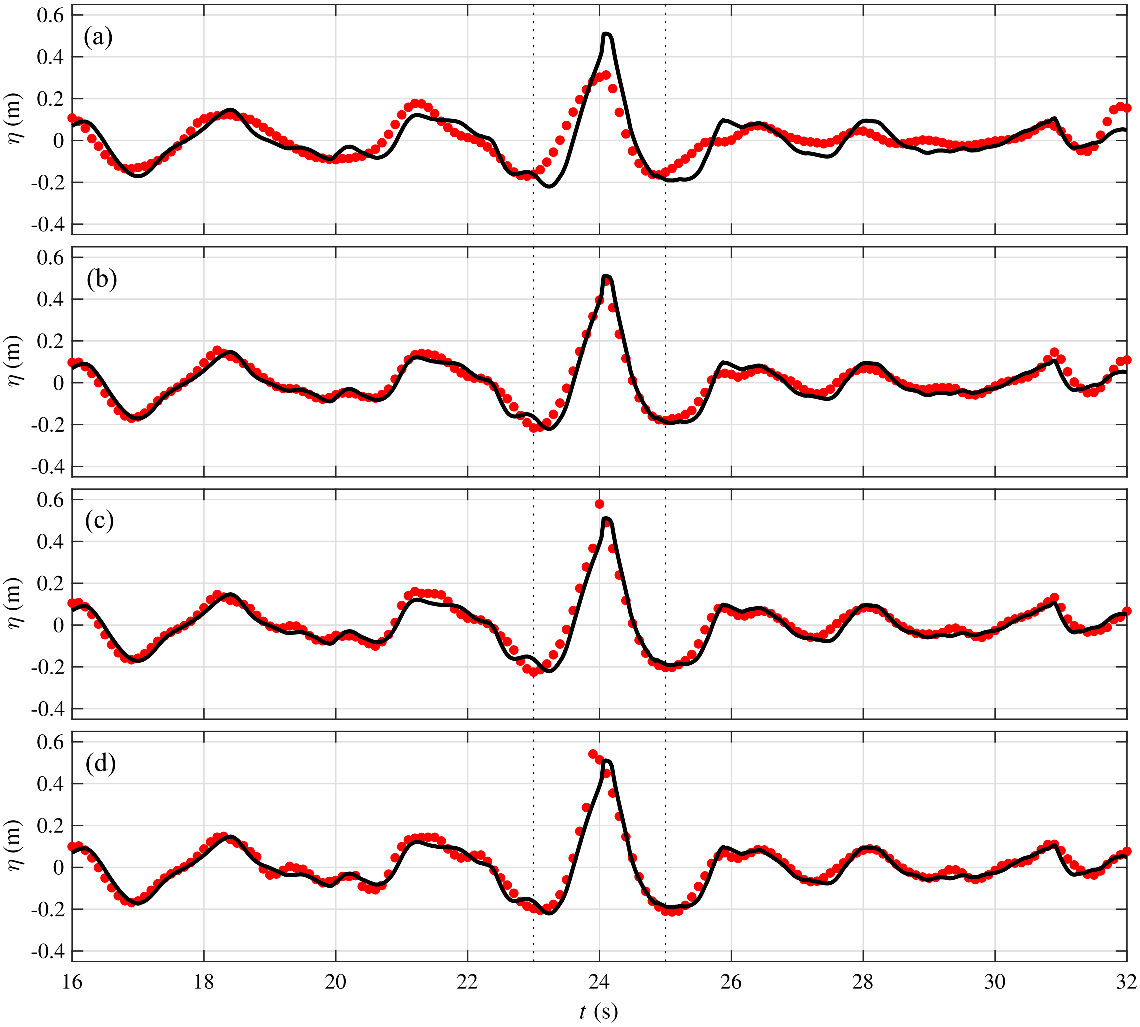

Fig. 6 Time series of surface elevation measured at wave gauge 4 ($x = 0$, $y = 0$) with four different h/d_p values of 1.4 (**a**), 1.7 (**b**), 2.0 (**c**), and 2.3 (**d**) in the crossing sea ($\Delta\theta = 120°$). Black lines denote the experimental measurements from MC19 and red dots the SPH results. Vertical dotted lines ($t = 23$–25 s) denote the time interval used to estimate r^2 in Fig. 7a, b. (Color figure online)

highly sensitive to model fidelity. So, instead, we draw comparison at the same instance in time. As h/d_p is increased, jet formation at the wave crest becomes more pronounced and moves forward (+ve x-direction). Qualitatively, the jet that forms when $h/d_p = 2.0$ is most similar to the experimental image. To fully reproduce small-scale features such as spray, a finer particle resolution would be required.

In Fig. 9, we display free surface elevation plotted along the x-axes at times $t = 23.5$, 24.0, and 24.5 s. Prior to wave focusing (a,d), simulated results show deviation from the experimental measurements for all values of h/d_p, particularly for $\Delta\theta = 120°$. However, at the time of focus and as the wave crest passes the gauges (b,c,e,f), the simulated surface elevation matches the measurements well (excluding $h/d_p = 1.4$). There are only subtle differences between the simulated wave crest around the time of maximum wave amplitude and breaking onset (b and e) for $h/d_p = 1.7$, 2.0 and 2.3. Visually, it appears that $h/d_p = 1.7$ provides the best agreement to the experiments for both crossing angles. We note, however, that when the free surface is very steep and potentially double valued, the gauge measurements may be less accurate (see also [53]), and drawing definitive conclusions on the basis of these subtle differences is challenging. For $h/d_p = 1.4$, large discrepancies are observed throughout the formation of the wave, and simulated wave crests are significantly smaller than the other simulations and experimental measurements.

3.3 Lagrangian particle accelerations

In this section, we analyse particle accelerations to investigate how varying h/d_p affects the onset, duration, and

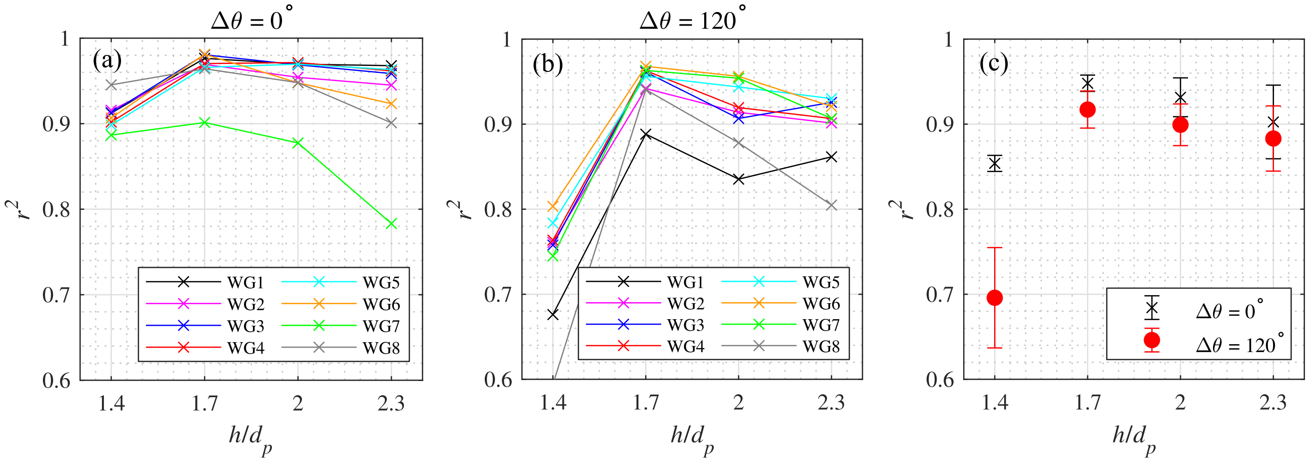

Fig. 7 Comparison of the r^2 values for four different h/d_p values. The surface elevations during the main crest (t =23–25 s) are used for calculation of the r^2 values in (**a, b**), and those during the entire simulations (0–32 s) in (**c**). In (**c**), the black crosses and red circles denote the r^2 values averaged over all the wave gauges, where error bars denote ± one standard deviation. (Color figure online)

spatial extent of breaking for both simulated experiments. Exploiting the outputs of the SPH model to examine the fluid particle accelerations directly allows for a comparative quantitative assessment of wave breaking behaviour, since the onset of breaking is not always visually apparent (e.g. Fig. 8g–j). This approach offers an alternative to applying established kinematic and dynamic criteria to assess breaking onset [71], which can be difficult to apply for crossing seas owing to the formation of partial standing waves and the difficulty associated with estimating crest velocity [64]. Here, we use normalised vertical particle acceleration $-a_z/g$ to indicate wave breaking, where particles with accelerations $-a_z/g \geq 1$ are in free fall (as observed experimentally in [72,73] for overturning waves).

Figures 10 and 11 show simulated free surface elevation, where particles for which $-a_z/g \geq 1$ are plotted using coloured markers. SPH particles are coloured red if $-a_z/g \geq 1$ at the timestamp plotted and are coloured blue if $-a_z/g \geq 1$ over the interval 22 to 28 s for $\Delta\theta = 0°$ and 22 to 26 s for $\Delta\theta = 120°$. To reduce computational time required for post processing, we limit the spatial domain over which we calculate $-a_z/g$ to $-2 \leq x \leq 7$, $-4 \leq y \leq 4$, $1.7 \leq z \leq 2.7$ for $\Delta\theta = 0°$ and to $-3 \leq x \leq 4$, $-3 \leq y \leq 3$, $1.7 \leq z \leq 2.7$ for $\Delta\theta = 120°$. These domains were chosen based on visual observation and capture the observed region of breaking for both cases. The timestamps are the same as those presented in Fig. 8, corresponding to times at which re-attachment occurs in Fig. 10 ($\Delta\theta = 0°$) and to the time of focus in Fig. 11 ($\Delta\theta = 120°$). Figure 12 presents the number of particles n_p for which $-a_z/g \geq 1$ as a function of time for all h/d_p values and both crossing angles.

When $\Delta\theta = 0°$ (Fig. 10), for all h/d_p values simulated a number of particles are in free fall, and it is evident that breaking is clearly initiated (also evident visually in Fig. 8b–e). The breaking crest, visualised using red markers in Fig. 10, takes a crescent shape owing to directional spreading. For the $h/d_p = 1.4$ simulation, the width of the breaking crest is smaller than the other simulations, as is the maximum crest amplitude, which is shown in Fig. 5a. These observations for $h/d_p = 1.4$ are likely a result of reduced fidelity in simulated wave focusing and dynamics owing to increased discretisation errors for lower values of h [74,75]. In Fig. 12a, the maximum number of particles with $-a_z/g \geq 1$ (indicative of the spatial extent of breaking) is significantly reduced for the $h/d_p = 1.4$ simulation compared to those with higher values of h/d_p; Fig. 12a demonstrates that the temporal and spatial extent of breaking is both reduced. For h/d_p values above 1.4, increasing h/d_p slightly delays the onset of breaking, whilst the total duration remains comparable. It is also noteworthy that for $h/d_p = 2.3$, there is a second peak in $n_p(t)$ (at $t = 25.3$ s), corresponding to an additional phase of breaking, which is less pronounced for lower values of h/d_p. The corresponding free surfaces are presented in Fig. 12c for the first and (d) for the second peak, showing the stages of wave breaking, as the overturning jet collides with the free surface.

For the simulations where $\Delta\theta = 120°$ (Fig. 11), wave breaking is more spatially localised than for $\Delta\theta = 0°$ (Fig. 10); the breaking crest front is smaller, and the total spatial extent of the breaking event is reduced for all smoothing lengths. As also observed in Fig. 10, increasing h/d_p appears to increase the number of particles with $-a_z/g \geq 1$. For $h/h_p = 1.4$, only 8 particles achieve free fall in the notably smaller crest that forms. Again, we believe that this

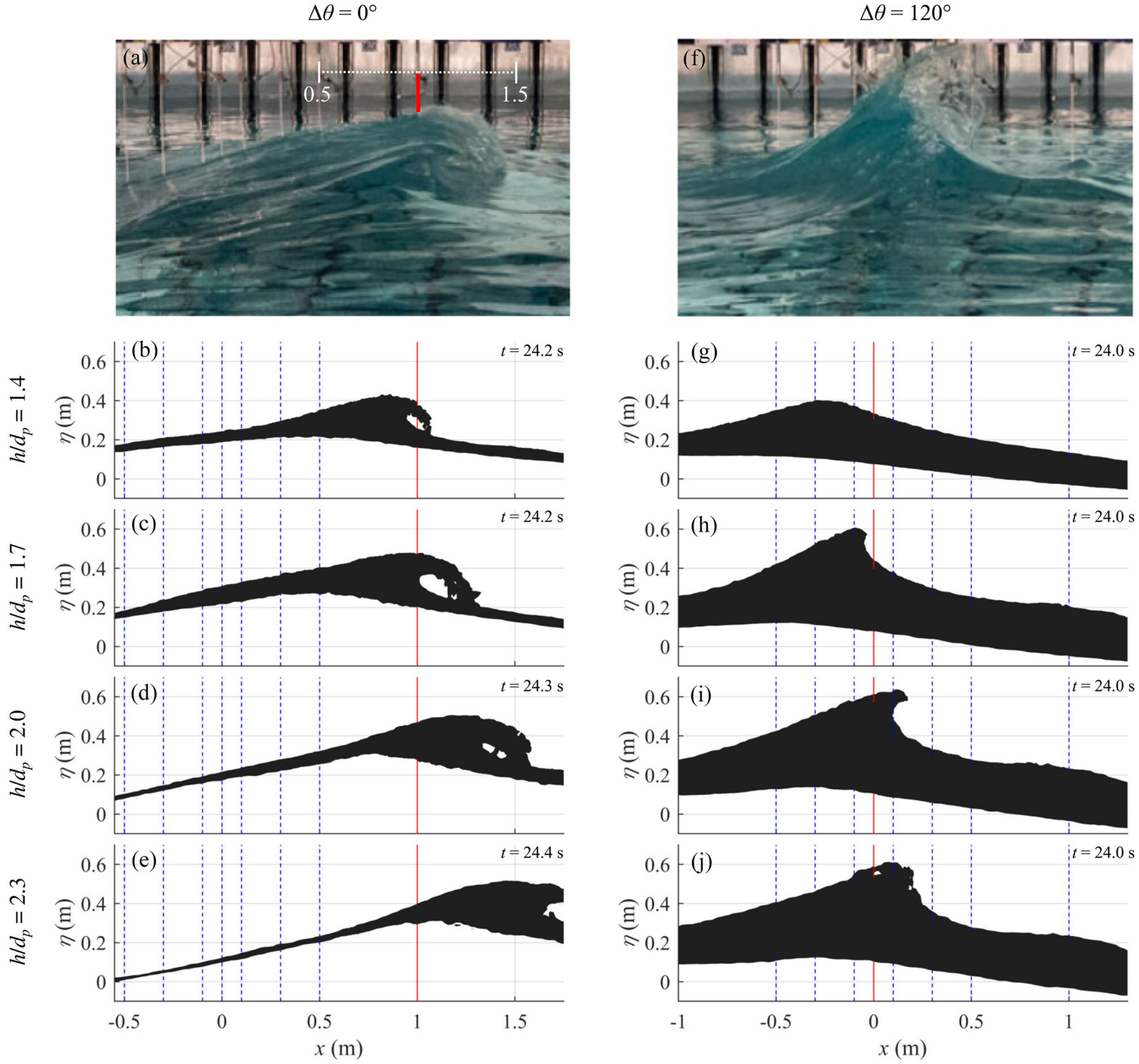

Fig. 8 Comparison of wave breaking between the experimental results of MC19 (**a, f**) and our simulations with four different h/d_p values of 1.4 (**b, g**), 1.7 (**c, h**), 2.0 (**d, i**), and 2.3 (**e, j**). (**a–e**) show the free surface in the following and (**f–j**) in the crossing sea. Wave gauges shown as blue dotted and red lines are ordered from left (wave gauge 1) to right (wave gauge 8). The red line marks wave gauge 8 in the following sea and wave gauge 4 in the crossing sea. All wave gauge positions shown as vertical lines align with those in (**a, f**). (Color figure online)

is a result of reduced model fidelity as a result of discretisation error [74,75]. Figure 12b further confirms observations that the number of particles in free fall is reduced for the $\Delta\theta = 120°$ case compared to $\Delta\theta = 0°$, and that significant breaking is not initiated for $h/d_p = 1.4$. For the largest value of h/d_p (2.3), there is a (marginal) secondary peak ($t = 24.9$ s) in $n_p(t)$, which is also observed in Fig. 12a for the $\Delta\theta = 0°$ case; this suggests that for both cases the second phase of breaking is better resolved for this higher value of h/d_p. In panel (e), partial breaking after the time of focus ($t = 24.5 > 24.0$ s) is shown, and the falling jet collides with free surface in panel (f). The spatial extent and duration of wave breaking for $h/d_p = 1.7$ is smaller than for higher h/d_p values and occurs slightly later. We note that $h/d_p = 1.7$ provides the best agreement with wave gauges (Figs. 5 and 6), which suggests that increasing smoothing length further may artificially increase the temporal and spatial extent of breaking for the scale we simulate. However, a more com-

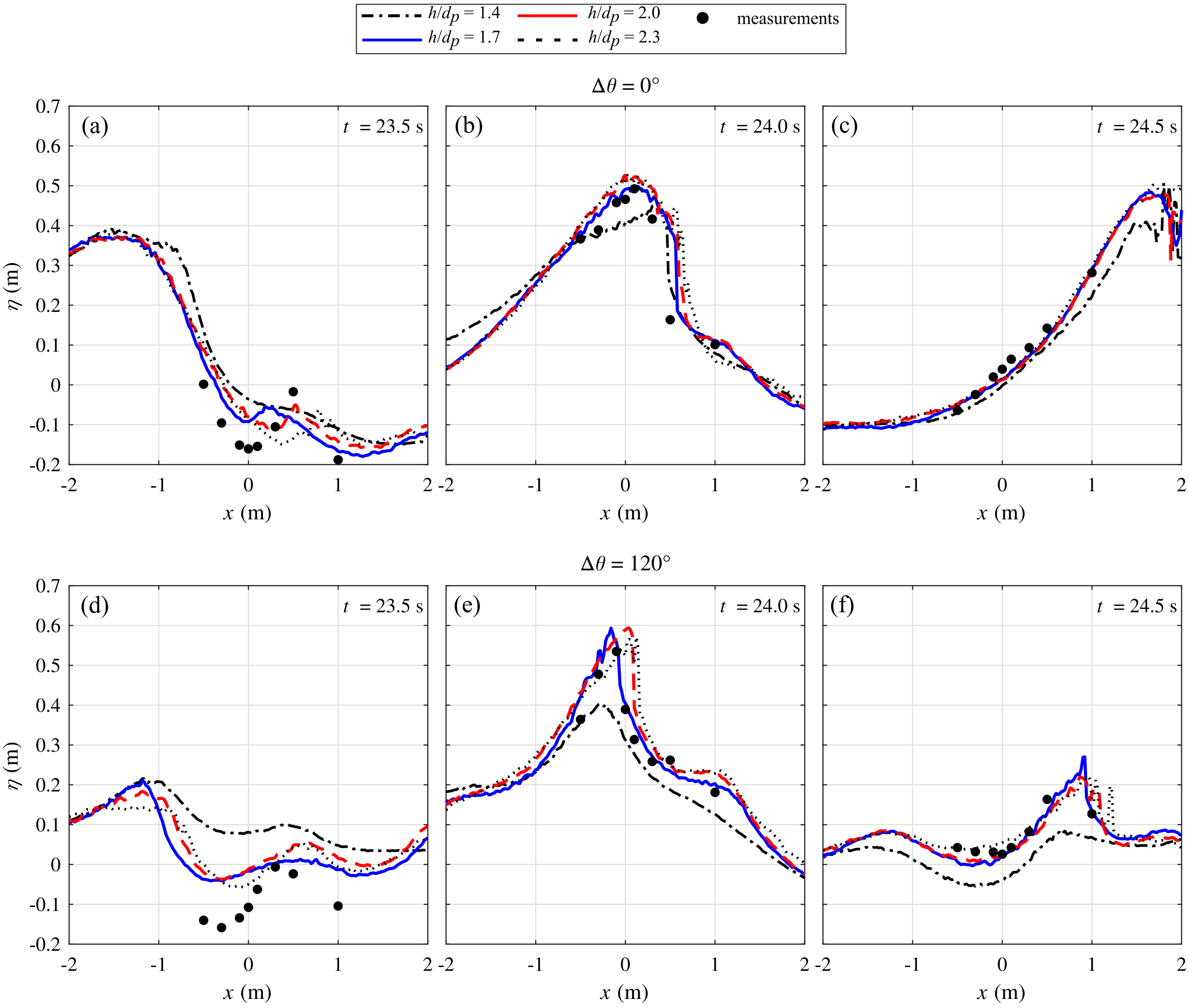

Fig. 9 Comparison of the free surface profiles between SPH results with four h/d_p values (lines) and experimental measurements (black circles) before the time of focus (**a, d**), at the time of focus (**b, e**) and after the time of focus (**c, f**). **a–c** The wave profiles in the following sea ($\Delta\theta = 0°$) and (**d, e, f**) in the crossing sea ($\Delta\theta = 120°$). (Color figure online)

prehensive comparison of simulations and experimental data is required to support this conclusion.

In summary, our results suggest that if h/d_p is too small, this limits the proper formation and focusing of the waves; the correct local steepness is not reached to initiate representative breaking. The effective lower limit on h/d_p appears to be dependent on the spatial localisation of the breaking event and hence is a function of directional spreading. When h is large relative to the scale of the breaking structures, then the onset of breaking can be delayed, and the duration of breaking increased, possibly to an unrepresentative level. The appropriate smoothing length h/d_p may be different when a different particle spacing d_p is used. In this study, we used a particle spacing of $H_D/d_p \approx 37$ and $\bar{H}/d_p = 12$, and a smoothing length h/d_p between 1.7 and 2.0 is recommended to best reproduce observed wave breaking.

4 Conclusions

We present a study in which we examine the effects of smoothing length h (which is normalised by particle spacing d_p) on SPH simulations of highly directionally spread following and crossing breaking waves. We carry out simulations using smoothing lengths h/d_p from 1.4 to 2.3. We perform simulations using the numerical wave tank detailed in [64,66,67] and reproduce the experiments presented in MC19, which allows for direct validation our results.

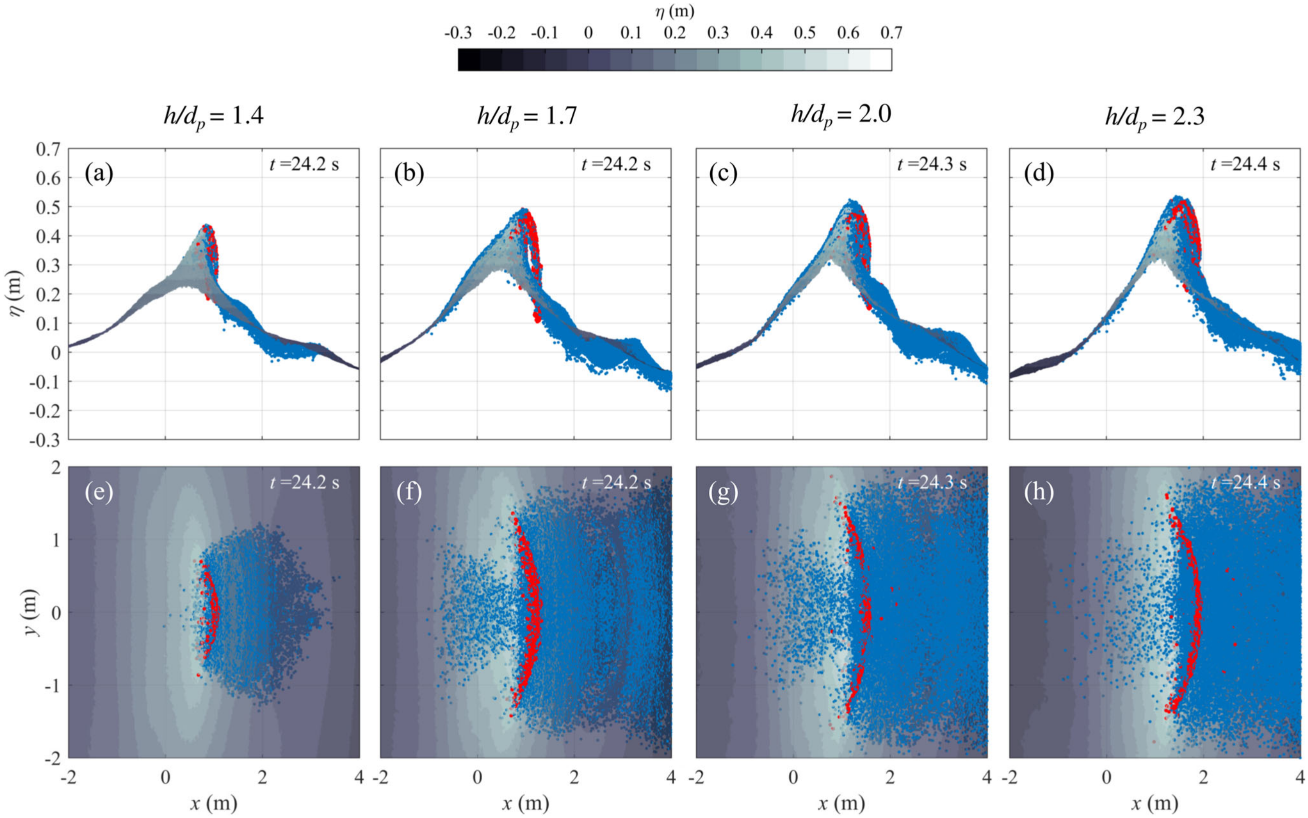

Fig. 10 Still images of the free surface for the following sea ($\Delta\theta = 0°$) with breaking particles highlighted using coloured markers. **a–d** Present the side view (z-x) and **e–h** the view from above (x-y). Particles are coloured red when $-a_z/g \geq 1$ at the time step presented, and blue when $-a_z/g \geq 1$ during the interval $t = 22.0–28.0$ s. (Color figure online)

To quantitatively assess the output of our simulations and the effects of smoothing length, we compare simulated surface elevation to measurements obtained in MC19 using values of the coefficient of determination r^2. The lowest smoothing length we used $h/d_p = 1.4$ resulted in under production of the experimental measurements (r^2 =0.70 for $\Delta\theta = 120°$ and 0.85 for $\Delta\theta = 0°$ in Fig. 7c). For $h/d_p = 1.7$ to 2.3 simulations reproduced experimental observations well, with values of r^2 ranging from approximately 0.88 to 0.95. Similarity between simulated and measured free surface elevation was greatest for $h/d_p = 1.7$, for which values of r^2 were greater than 0.9 for both $\Delta\theta = 120°$ and $\Delta\theta = 0°$. Values of r^2 were consistently lower for the crossing simulations ($\Delta\theta = 120°$), which may be a result of the spatial localisation of the waves in these experiments. In the simulations of following waves ($\Delta\theta = 0°$) with smoothing lengths $h/d_p = 1.7$ to 2.3, r^2 values show that the effects of smoothing length are most pronounced at wave gauges 6, 7, and 8, where wave breaking has occurred. We note at these gauges the process of wave breaking may introduce error in the measurements recorded.

To examine the effects of smoothing length on simulated wave breaking in more detail, we perform a qualitative comparison of wave breaking phenomena observed in experiments and simulations. For the following waves ($\Delta\theta = 0°$), the re-attachment of the plunging jet and position of the forward face of the wave simulated for values of $h/d_p = 1.7$ and 2.0 provided the closest match to experiments. For larger values of h/d_p, the location of re-attachment moves forward (+ve x-direction) and occurs later than in the experiments. For the crossing waves $\Delta\theta = 120°$, clear re-attachment of the jet does not occur, so visual comparison is more challenging. The shape and position of the crest in these simulations also suggest wave breaking is best reproduced using smoothing lengths of $h/d_p = 1.7$ and 2.0.

In our simulations with $\Delta\theta = 120°$, the onset of wave breaking is difficult to identify from visual observation alone. We use vertical acceleration of fluid particles to asses when breaking may be occurring and gain additional insight into how smoothing length h/d_p affects simulated breaking. We investigated the number of particles whose vertical acceleration reaches $-g$ as an indication of free-falling fluid

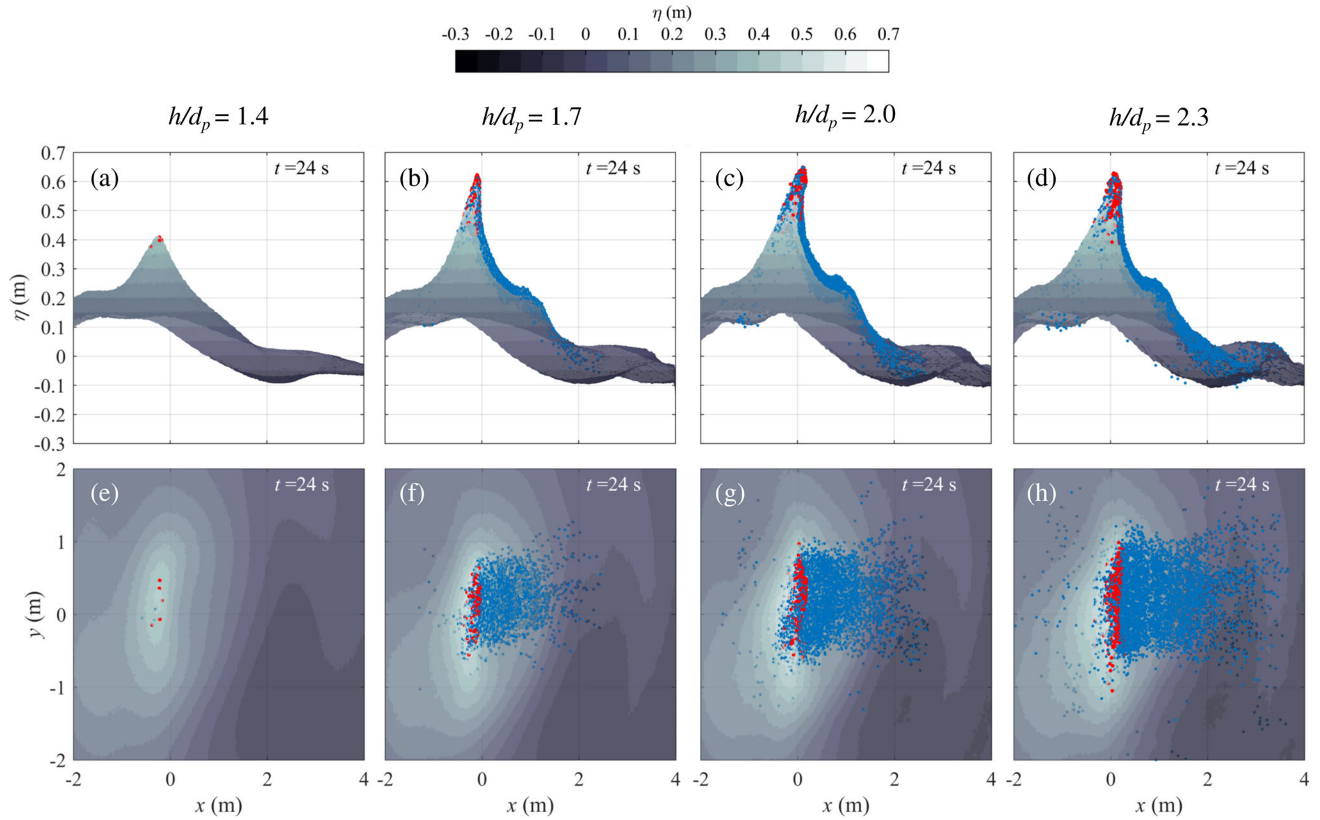

Fig. 11 Still images of the free surface for the crossing sea ($\Delta\theta = 120°$) with breaking particles highlighted using coloured markers. **a–d** Present the side view (z-x) and **e–h** view from above (x-y). Particles are coloured red when $-a_z/g \geq 1$ at the time step presented, and blue when $-a_z/g \geq 1$ during the interval 22.0 to 26.0 s. (Color figure online)

and hence breaking. The number of free-falling particles observed in the simulations indicates that varying smoothing length affects the spatial extent and duration of wave breaking. For $h/d_p = 1.4$, the spatial and temporal extent of breaking is considerably reduced for $\Delta\theta = 0°$, and breaking may not even be occurring for $\Delta\theta = 120°$. For $h/d_p = 1.7$ to 2.3, the duration of an spatial extent of breaking increases with smoothing length. For $\Delta\theta = 0°$, increasing smoothing length also appears to slightly delay the onset of breaking. For the largest smoothing length $h/d_p = 2.3$, a secondary peak in the number of free-falling particles occurs in both simulations ($\Delta\theta = 0°$ and $\Delta\theta = 120°$), corresponding to a second stage of wave breaking, in which the falling jet collides with the surface upon re-attachment.

Our comparison of simulations and experiments demonstrates the sensitivity of simulated wave breaking to the choice of smoothing length. The lowest value we use $h/d_p = 1.4$ fails to reproduce the experimental measurements and observed wave breaking. This low smoothing length may introduce greater discretisation errors due to the lower number of particles in the kernel's support [74,75]. We believe that this affects the fidelity of the simulated surface motion and results in failure to recreate conditions in the physical wave tank that lead to the formation of the larger wave crest. At smoothing lengths of $h/d_p = 1.7$ to 2.3, prior to wave breaking, the simulated results are similar and less sensitive to smoothing length. Increasing smoothing length appears to increase the duration and spatial extent of breaking. Thus, the true extent of breaking may be overestimated when deriving physical quantities using a smoothing length which is too large relative to the length scale of breaking structures.

The SPH model presented is capable of reproducing the large focused waves with their different breaking behaviours in highly directionally spread (following and crossing) conditions. Based on the results we present, we recommend using h/d_p between 1.7 and 2.0. It should be noted that the appropriate h/d_p value may vary for different values of particle spacing d_p and different numerical schemes. (In our simulations $H_D/d_p = 37$, and we have used WCSPH, delta-SPH [36], and a Wendland kernel.) Other sensitive studies for h/dp can be found in [7,53,54]. To examine the effects of smoothing length fully, we recommend that a comprehensive

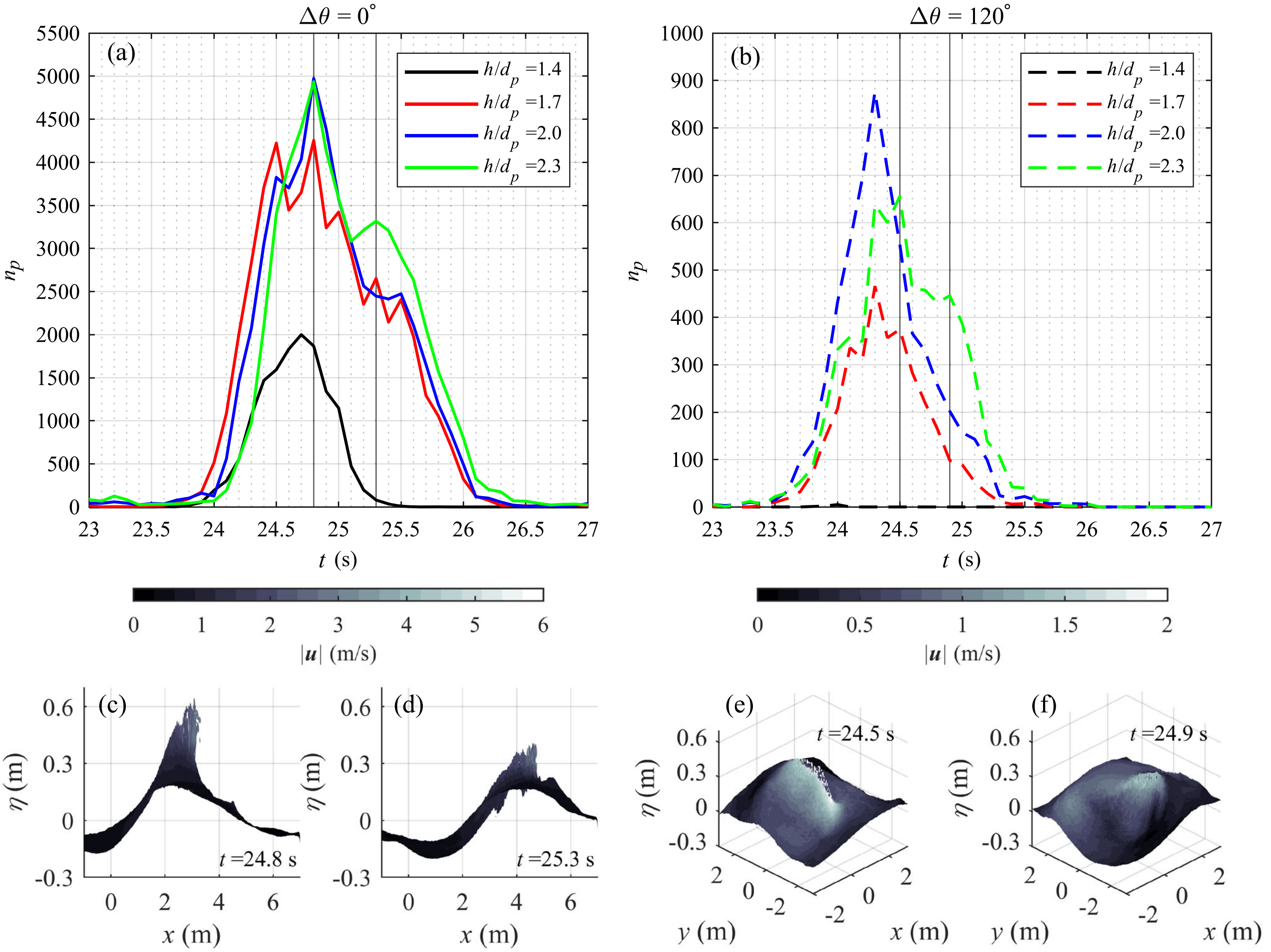

Fig. 12 Time series of the instantaneous number of particles (n_p) with $-a_z/g \geq 1$ for four different h/d_p values and two crossing angles $\Delta\theta$ (**a, b**). The vertical black lines denote the time of the first and second peak of n_p for $h/d_p = 2.3$. The corresponding free surface elevations are shown in (**c–f**). (Color figure online)

study of breaking and non-breaking waves is carried out in which both h and d_p are varied independently.

Acknowledgements The authors acknowledge support from JSPS KAKENHI Grant Number 19J13966, 20K22396, and 20H02369. TSvdB acknowledges support from a Royal Academy of Engineering Research Fellowship.

Declarations

Conflict of interest The authors declare that they have no conflict of interest.

References

1. Babanin A (2011) Breaking and dissipation of ocean surface waves. Cambridge University Press, Cambridge. https://doi.org/10.1017/CBO9780511736162
2. Khayyer A, Gotoh H (2008) Development of CMPS method for accurate water-surface tracking in breaking waves. Coast Eng J 50(2):179–207. https://doi.org/10.1142/S0578563408001788
3. Saruwatari A, Watanabe Y, Ingram DM (2009) Scarifying and fingering surfaces of plunging jets. Coast Eng 56(11):1109–1122. https://doi.org/10.1016/j.coastaleng.2009.08.007
4. Xie J, Nistor I, Murty T (2012) A corrected 3-D SPH method for breaking tsunami wave modelling. Nat Hazards 60(1):81–100
5. He F, Zhang H, Huang C, Liu M (2020) Numerical investigation of the solitary wave breaking over a slope by using the finite particle method. Coast Eng 156:103617. https://doi.org/10.1016/j.coastaleng.2019.103617

6. Wei Z, Dalrymple RA, Xu M, Garnier R, Derakhti M (2017) Short-crested waves in the surf zone. J Geophys Res Oceans 122(5):4143–4162. https://doi.org/10.1002/2016JC012485
7. Lowe R, Buckley M, Altomare C, Rijnsdorp D, Yao Y, Suzuki T, Bricker J (2019) Numerical simulations of surf zone wave dynamics using Smoothed Particle Hydrodynamics. Ocean Model 144:101481. https://doi.org/10.1016/j.ocemod.2019.101481
8. Mostert W, Deike L (2020) Inertial energy dissipation in shallow-water breaking waves. J Fluid Mech 890:A12. https://doi.org/10.1017/jfm.2020.83
9. De Padova D, Ben Meftah M, De Serio F, Mossa M, Sibilla S (2020) Characteristics of breaking vorticity in spilling and plunging waves investigated numerically by SPH. Environ Fluid Mech 20(2):233–260. https://doi.org/10.1007/s10652-019-09699-5
10. Lin P, Liu PLF (1998) A numerical study of breaking waves in the surf zone. J Fluid Mech 359(1):239–264
11. Jose J, Choi SJ, Giljarhus KET, Gudmestad OT (2017) A comparison of numerical simulations of breaking wave forces on a monopile structure using two different numerical models based on finite difference and finite volume methods. Ocean Eng 137:78–88
12. Sun PN, Luo M, Le Touzé D, Zhang AM (2019) The suction effect during freak wave slamming on a fixed platform deck: smoothed particle hydrodynamics simulation and experimental study. Phys Fluids 31(11):117108
13. Yan B, Luo M, Bai W (2019) An experimental and numerical study of plunging wave impact on a box-shape structure. Mar Struct 66:272–287
14. Chen X, Chen Q, Chen Z, Cai S, Zhuo X, Lv J (2021) Numerical modeling of the interaction between submerged floating tunnel and surface waves. Ocean Eng 220:108494
15. Luo M, Khayyer A, Lin P (2021) Particle methods in ocean and coastal engineering. Appl Ocean Res 114:102734. https://doi.org/10.1016/j.apor.2021.102734
16. Sun PN, Le Touzé D, Oger G, Zhang AM (2021) An accurate FSI-SPH modeling of challenging fluid-structure interaction problems in two and three dimensions. Ocean Eng 221:108552. https://doi.org/10.1016/j.oceaneng.2020.108552
17. Violeau D, Rogers BD (2016) Smoothed particle hydrodynamics (SPH) for free-surface flows: past, present and future. J Hydraul Res 54(1):1–26. https://doi.org/10.1080/00221686.2015.1119209
18. Hirt C, Nichols B (1981) Volume of fluid (VOF) method for the dynamics of free boundaries. J Comput Phys 39(1):201–225. https://doi.org/10.1016/0021-9991(81)90145-5
19. Osher S, Sethian JA (1988) Fronts propagating with curvature-dependent speed: algorithms based on Hamilton–Jacobi formulations. J Comput Phys 79(1):12–49. https://doi.org/10.1016/0021-9991(88)90002-2
20. Scardovelli R, Zaleski S (1999) Direct numerical simulation of free-surface and interfacial flow. Annu Rev Fluid Mech 31(1):567–603. https://doi.org/10.1146/annurev.fluid.31.1.567
21. Lucy LB (1977) A numerical approach to the testing of the fission hypothesis. Astron J 82:1013–1024. https://doi.org/10.1086/112164
22. Gingold RA, Monaghan JJ (1977) Smoothed particle hydrodynamics: theory and application to non-spherical stars. Mon Not R Astron Soc 181(3):375–389. https://doi.org/10.1093/mnras/181.3.375
23. Koshizuka S (1995) A particle method for incompressible viscous flow with fluid fragmentation. Comput Fluid Dyn J 4:29–46
24. Altomare C, Domínguez J, Crespo A, González-Cao J, Suzuki T, Gómez-Gesteira M, Troch P (2017) Long-crested wave generation and absorption for SPH-based DualSPHysics model. Coast Eng 127:37–54. https://doi.org/10.1016/j.coastaleng.2017.06.004
25. Draycott S, Li Y, Stansby P, Adcock T, van den Bremer T (2022) Harmonic-induced wave breaking due to abrupt depth transitions: an experimental and numerical study. Coast Eng 171:104041. https://doi.org/10.1016/j.coastaleng.2021.104041
26. Crespo A, Gómez-Gesteira M, Dalrymple R (2007) Boundary conditions generated by dynamic particles in SPH methods. Comput Mater Contin 5(3):173–184
27. Monaghan J (1994) Simulating free surface flows with SPH. J Comput Phys 110(2):399–406. https://doi.org/10.1006/jcph.1994.1034
28. Lo EY, Shao S (2002) Simulation of near-shore solitary wave mechanics by an incompressible SPH method
29. Chorin AJ (1968) Numerical solution of the Navier–Stokes equations. Math Comput 22(104):745–762
30. Shadloo MS, Zainali A, Yildiz M, Suleman A (2012) A robust weakly compressible SPH method and its comparison with an incompressible SPH. Int J Numer Methods Eng 89(8):939–956. https://doi.org/10.1002/nme.3267
31. Hérault A, Bilotta G, Dalrymple RA (2010) SPH on GPU with CUDA. J Hydraul Res 48(sup1):74–79. https://doi.org/10.1080/00221686.2010.9641247
32. Cercos-Pita J (2015) Aquagpusph, a new free 3D SPH solver accelerated with OPENCL. Comput Phys Commun 192:295–312. https://doi.org/10.1016/j.cpc.2015.01.026
33. Antuono M, Colagrossi A, Marrone S (2012) Numerical diffusive terms in weakly-compressible SPH schemes. Comput Phys Commun 183(12):2570–2580. https://doi.org/10.1016/j.cpc.2012.07.006
34. Monaghan J, Gingold R (1983) Shock simulation by the particle method SPH. J Comput Phys 52(2):374–389. https://doi.org/10.1016/0021-9991(83)90036-0
35. Belytschko T, Xiao S (2002) Stability analysis of particle methods with corrected derivatives. Comput Math Appl 43(3):329–350. https://doi.org/10.1016/S0898-1221(01)00290-5
36. Molteni D, Colagrossi A (2009) A simple procedure to improve the pressure evaluation in hydrodynamic context using the SPH. Comput Phys Commun 180(6):861–872. https://doi.org/10.1016/j.cpc.2008.12.004
37. Lind SJ, Rogers BD, Stansby PK (2020) Review of smoothed particle hydrodynamics: towards converged Lagrangian flow modelling. Proc R Soc A Math Phys Eng Sci 476(2241):20190801. https://doi.org/10.1098/rspa.2019.0801
38. Monaghan J (2000) SPH without a tensile instability. J Comput Phys 159(2):290–311. https://doi.org/10.1006/jcph.2000.6439
39. Sun PN, Colagrossi A, Zhang AM (2018) Numerical simulation of the self-propulsive motion of a fishlike swimming foil using the δ^+-SPH model. Theor Appl Mech Lett 8(2):115–125. https://doi.org/10.1016/j.taml.2018.02.007
40. Lyu HG, Sun PN (2022) Further enhancement of the particle shifting technique: towards better volume conservation and particle distribution in SPH simulations of violent free-surface flows. Appl Math Model 101:214–238. https://doi.org/10.1016/j.apm.2021.08.014
41. Sun P, Colagrossi A, Marrone S, Antuono M, Zhang A (2018) Multi-resolution delta-plus-SPH with tensile instability control: towards high Reynolds number flows. Comput Phys Commun 224:63–80. https://doi.org/10.1016/j.cpc.2017.11.016
42. Xu X, Yu P (2018) A technique to remove the tensile instability in weakly compressible SPH. Comput Mech 62(5):963–990. https://doi.org/10.1007/s00466-018-1542-4
43. You Y, Khayyer A, Zheng X, Gotoh H, Ma Q (2021) Enhancement of δ-SPH for ocean engineering applications through incorporation of a background mesh scheme. Appl Ocean Res 110:102508. https://doi.org/10.1016/j.apor.2020.102508
44. Koshizuka S, Nobe A, Oka Y (1998) Numerical analysis of breaking waves using the moving particle semi-implicit method. Int J Numer Methods Fluids 26(7):751–769. https://doi.org/10.1002/(SICI)1097-0363(19980415)26:7<751::AID-FLD671>3.0.CO;2-C

45. Monaghan JJ, Kos A (1999) Solitary waves on a Cretan beach. J Waterw Port Coast Ocean Eng 125(3):145–155. https://doi.org/10.1061/(ASCE)0733-950X(1999)125:3(145)
46. Farahani RJ, Dalrymple RA (2014) Three-dimensional reversed horseshoe vortex structures under broken solitary waves. Coast Eng 91:261–279. https://doi.org/10.1016/j.coastaleng.2014.06.006
47. Meringolo DD, Liu Y, Wang XY, Colagrossi A (2018) Energy balance during generation, propagation and absorption of gravity waves through the δ-LES-SPH model. Coast Eng 140:355–370. https://doi.org/10.1016/j.coastaleng.2018.07.007
48. Gotoh H (2001) Sub-particle-scale turbulence model for the MPS method-Lagrangian flow model for hydraulic engineering. Comput Fluid Dyn J 9(4):339–347
49. Dalrymple R, Rogers B (2006) Numerical modeling of water waves with the SPH method. Coast Eng 53(2):141–147. https://doi.org/10.1016/j.coastaleng.2005.10.004
50. Crespo AJ, Domínguez JM, Rogers BD, Gómez-Gesteira M, Longshaw S, Canelas R, Vacondio R, Barreiro A, García-Feal O (2015) DualSPHysics: open-source parallel CFD solver based on smoothed particle hydrodynamics (SPH). Comput Phys Commun 187:204–216. https://doi.org/10.1016/j.cpc.2014.10.004
51. Roselli RAR, Vernengo G, Brizzolara S, Guercio R (2019) SPH simulation of periodic wave breaking in the surf zone—a detailed fluid dynamic validation. Ocean Eng 176:20–30. https://doi.org/10.1016/j.oceaneng.2019.02.013
52. Khayyer A, Gotoh H, Shao S (2008) Corrected Incompressible SPH method for accurate water-surface tracking in breaking waves. Coast Eng 55(3):236–250. https://doi.org/10.1016/j.coastaleng.2007.10.001
53. Padova DD, Dalrymple RA, Mossa M (2014) Analysis of the artificial viscosity in the smoothed particle hydrodynamics modelling of regular waves. J Hydraul Res 52(6):836–848. https://doi.org/10.1080/00221686.2014.932853
54. Rota Roselli RA, Vernengo G, Altomare C, Brizzolara S, Bonfiglio L, Guercio R (2018) Ensuring numerical stability of wave propagation by tuning model parameters using genetic algorithms and response surface methods. Environ Model Softw 103:62–73. https://doi.org/10.1016/j.envsoft.2018.02.003
55. Forristall GZ, Ewans KC (1998) Worldwide measurements of directional wave spreading. J Atmos Ocean Tech 15(2):440–469
56. Goda Y (1999) A comparative review on the functional forms of directional wave spectrum. Coast Eng J 41(1):1–20. https://doi.org/10.1142/S0578563499000024
57. Toffoli A, Lefèvre J, Bitner-Gregersen E, Monbaliu J (2005) Towards the identification of warning criteria: analysis of a ship accident database. Appl Ocean Res 27(6):281–291. https://doi.org/10.1016/j.apor.2006.03.003
58. Cavaleri L, Bertotti L, Torrisi L, Bitner-Gregersen E, Serio M, Onorato M (2012) Rogue waves in crossing seas: the Louis Majesty accident. J Geophys Res Oceans. https://doi.org/10.1029/2012JC007923
59. Trulsen K, Nieto Borge JC, Gramstad O, Aouf L, Lefèvre J (2015) Crossing sea state and rogue wave probability during the prestige accident. J Geophys Res Oceans 120(10):7113–7136. https://doi.org/10.1002/2015JC011161
60. Zhang Z, Li XM (2017) Global ship accidents and ocean swell-related sea states. Nat Hazard 17(11):2041–2051. https://doi.org/10.5194/nhess-17-2041-2017
61. McAllister ML, Draycott S, Adcock TAA, Taylor PH, van den Bremer TS (2019) Laboratory recreation of the Draupner wave and the role of breaking in crossing seas. J Fluid Mech 860:767–786. https://doi.org/10.1017/jfm.2018.886
62. Haver S (2004) A possible freak wave event measured at the Draupner Jacket, January 1 1995. Brest
63. Ingram D, Wallace R, Robinson A, Bryden I (2014) The design and commissioning of the first, circular, combined current and wave test basin. In: Proceedings of oceans 2014 MTS/IEEE Taipei, Taiwan. Institute of Electrical and Electronics Engineers (IEEE), United States
64. Kanehira T, McAllister M, Draycott S, Nakashima T, Taniguchi N, Ingram D, van den Bremer T, Mutsuda H (2021) Highly directionally spread, overturning breaking waves modelled with Smoothed Particle Hydrodynamics: A case study involving the Draupner wave. Ocean Model. https://doi.org/10.1016/j.ocemod.2021.101822
65. Domínguez JM, Fourtakas G, Altomare C, Canelas RB, Tafuni A, García-Feal O, Martínez-Estévez I, Mokos A, Vacondio R, Crespo AJ et al (2021) DualSPHysics: from fluid dynamics to multiphysics problems. Comput Particle Mech 25:1–25
66. Kanehira T, Mutsuda H, Doi Y, Taniguchi N, Draycott S, Ingram D (2019) Development and experimental validation of a multidirectional circular wave basin using smoothed particle hydrodynamics. Coast Eng J 61(1):109–120. https://doi.org/10.1080/21664250.2018.1560922
67. Kanehira T, Mutsuda H, Draycott S, Taniguchi N, Nakashima T, Doi Y, Ingram D (2020) Numerical re-creation of multi-directional waves in a circular basin using a particle based method. Ocean Eng 209:107446. https://doi.org/10.1016/j.oceaneng.2020.107446
68. Wendland H (1995) Piecewise polynomial, positive definite and compactly supported radial functions of minimal degree. Adv Comput Math 4(1):389–396. https://doi.org/10.1007/BF02123482
69. Lo EY, Shao S (2002) Simulation of near-shore solitary wave mechanics by an incompressible SPH method. Appl Ocean Res 24(5):275–286. https://doi.org/10.1016/S0141-1187(03)00002-6
70. Leimkuhler B, Patrick GW (1996) A symplectic integrator for Riemannian manifolds. J Nonlinear Sci 6(4):367–384. https://doi.org/10.1007/BF02433475
71. Perlin M, Choi W, Tian Z (2013) Breaking waves in deep and intermediate waters. Annu Rev Fluid Mech 45(1):115–145. https://doi.org/10.1146/annurev-fluid-011212-140721
72. Chang KA, Liu PLF (1998) Velocity, acceleration and vorticity under a breaking wave. Phys Fluids 10(1):327–329. https://doi.org/10.1063/1.869544
73. Grue J, Jensen A (2006) Experimental velocities and accelerations in very steep wave events in deep water. Eur J Mech B/Fluids 25(5):554–564
74. Quinlan NJ, Basa M, Lastiwka M (2006) Truncation error in mesh-free particle methods. Int J Numer Methods Eng 66(13):2064–2085. https://doi.org/10.1002/nme.1617
75. Oger G, Doring M, Alessandrini B, Ferrant P (2007) An improved SPH method: towards higher order convergence. J Comput Phys 225(2):1472–1492. https://doi.org/10.1016/j.jcp.2007.01.039